

Theory of Scanning Tunneling Spectroscopy of a Magnetic Adatom on a Metallic Surface

Avraham Schiller¹ and Selman Hershfield²

¹ *Racah Institute of Physics, The Hebrew University, Jerusalem 91904, Israel*

² *Department of Physics and National High Magnetic Field Laboratory, University of Florida,
PO Box 118440, Gainesville, FL 32611*

(June 19, 2018)

A comprehensive theory is presented for the voltage, temperature, and spatial dependence of the tunneling current between a scanning tunneling microscope (STM) tip and a metallic surface with an individual magnetic adatom. Modeling the adatom by a nondegenerate Anderson impurity, a general expression is derived for a weak tunneling current in terms of the dressed impurity Green function, the impurity-free surface Green function, and the tunneling matrix elements. This generalizes Fano's analysis to the interacting case. The differential-conductance lineshapes seen in recent STM experiments with the tip directly over the magnetic adatom are reproduced within our model, as is the rapid decay, $\sim 10\text{\AA}$, of the low-bias structure as one moves the tip away from the adatom. With our simple model for the electronic structure of the surface, there is no dip in the differential conductance at approximately one lattice spacing from the magnetic adatom, but rather we see a resonant enhancement. The formalism for tunneling into small clusters of magnetic adatoms is developed.

PACS numbers: 72.15.Qm, 61.16.Ch, 72.10.Fk

I. INTRODUCTION

Recently, a scanning tunneling microscope (STM) was used in two separate experiments^{1,2} to directly probe the local electronic structure of an isolated magnetic adatom on a metallic surface. By measuring the tunneling current from the substrate to the STM tip, a narrow resonant feature was seen in the differential conductance when the tip was placed directly above the magnetic adatom: an antiresonance in the case of a cerium adatom on the (111) surface of silver,¹ and an asymmetric Fano resonance in the case of a cobalt adatom on the (111) surface of gold.² These resonant structures gradually disappeared upon removing the tip from the adatom. Specifically, the asymmetric lineshape for Co on Au(111) first evolved into a more symmetric dip, before disappearing altogether at a lateral distance of about 12\AA from the Co adatom.² Both experiments were interpreted as a manifestation of the Kondo resonance that develops due to the screening of the local moment on the magnetic adatom by the substrate conduction electrons.

While similar observations of the Kondo effect for a single magnetic impurity were recently reported both in quantum dots^{3,4} and in metallic point contacts,⁵ STM spectroscopy offers the unique ability to spatially resolve the electronic structure around the magnetic adatom. This provides direct information about the screening of the local moment, allowing for critical comparison between theory and experiment. Another novel aspect of STM spectroscopy in this context is the quantum-mechanical interference between direct tunneling into the magnetic adatom and tunneling into the underlying substrate conduction electrons, as first discussed by Fano⁶ for the noninteracting case. For a quantum dot placed in

between two metallic leads, the analogous interference is between Kondo-assisted tunneling through the dot and direct tunneling between the leads, the latter being extremely small.

Motivated by the recent STM experiments, this paper provides a comprehensive theory for the voltage, temperature, and spatial dependence of the tunneling current between an STM tip and a metallic surface with an individual magnetic adatom. Modeling the adatom by a nondegenerate Anderson impurity, a general expression is derived for a weak tunneling current in terms of the fully dressed impurity Green function and the impurity-free surface Green function. The impurity Green function is evaluated in turn using the non-crossing approximation (NCA), while the surface Green function is obtained within a tight-binding model with free boundary condition at the surface. This allows for a consistent description of the energy and the spatial dependence of the tunneling current, as is required in this case. Both cases of point tunneling and that of a finite spatial extent in the tunneling matrix element between the tip and the substrate conduction electrons are considered within this model.

As expected of the Kondo effect, a sharp resonant structure is found to develop in the low-voltage differential conductance as the temperature is lowered down to the Kondo temperature, T_K . The width of the resonance is proportional to T_K at low temperatures, growing with T for $T > T_K$. Its shape is governed by a single interference parameter q , much in the same way as in the noninteracting case.⁶ The value of q and its spatial variation depends quite sensitively on details of the underlying surface Green function and the tunneling matrix elements, which limits the direct applicability of our re-

sults to the experimental data. Nevertheless, we are able to make some qualitative statements regarding the experiment. In particular, the indirect interference with the magnetic adatom, i.e., that due to the tunneling between the STM tip and the underlying conduction electrons, is found to have a characteristic range of the order of two lattice spacings, consistent with the limited spatial extent of the Kondo resonance in the experiment. In addition, the spatial dependence of the differential conductance as measured for Co on Au(111)² is shown to be nongeneric, indicating a crucial dependence on the microscopic details of the (111) surface of gold. Finally, since the widths of the resonant features in Refs. 1 and 2 are both notably larger than the temperature, we conclude that $T < T_K$ in both experiments.

The remainder of the paper is organized as follows: In Sec. II the basic model is introduced, and a general expression is derived for the differential conductance in the limit of a weak tunneling current. Sec. III then details our calculation scheme for the dressed impurity Green function and the impurity-free surface Green function. Simplified expressions for the first few nonlocal surface Green functions of our model are provided in Appendix A. Results for the voltage, temperature, and spatial dependence of the low-voltage differential conductance are presented in turn in sections IV and V, with Sec. IV dedicated to the case of point tunneling between the STM tip and the underlying substrate conduction electrons, and Sec. V devoted to the case of a spatially extended matrix element for tunneling. The main results of the paper are finally summarized in Sec. VI, followed by a brief comparison with previous work in Appendix B, and a generalization of our approach to the case of multiple magnetic adatoms in Appendix C.

II. MODEL AND TUNNELING CURRENT

The system under consideration is shown schematically in Fig. 1. It consists of an individual magnetic adatom, modeled by a d level with energy ϵ_d and an on-site repulsion U , deposited on top of a metallic surface. The d electrons hybridize locally with the underlying conduction electrons via the matrix element V_h . This setting is probed by an STM tip which is placed directly above the surface point \vec{R}_s , and which couples separately to the d electrons and to the local conduction electrons at site \vec{R}_i through the tunneling matrix elements t_d and t_c , respectively. The adatom is taken to be positioned at \vec{R}_i . An applied voltage bias between the substrate and the tip offsets the two chemical potentials, $\mu_{tip} - \mu_{sub} = eV$, causing a weak electrical current to flow between the substrate and the tip.

Setting the substrate chemical potential as our reference energy, the corresponding Hamiltonian takes the form $\mathcal{H} = \mathcal{H}_{sub} + \mathcal{H}_{tip} + \mathcal{H}_{tun}$, where

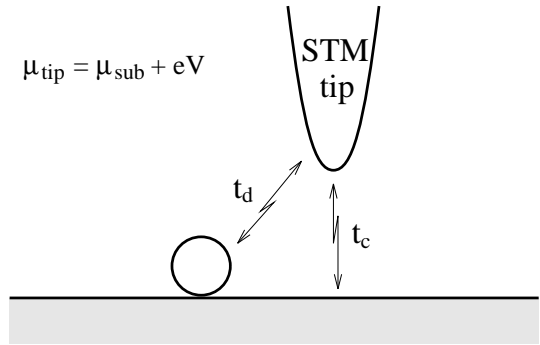


FIG. 1. Schematic description of the physical system. A metallic surface with an individual magnetic adatom is probed by an STM tip. The tip couples separately to the atomic d electrons and to the underlying conduction electrons via the tunneling matrix elements t_d and t_c , respectively. A voltage bias is applied between the sample and the STM tip, causing a weak electrical current to flow between the substrate and the tip.

$$\begin{aligned} \mathcal{H}_{sub} = & \sum_{\vec{k}\sigma} \epsilon_{\vec{k}} c_{\vec{k}\sigma}^\dagger c_{\vec{k}\sigma} + \epsilon_d \sum_{\sigma} d_{\sigma}^\dagger d_{\sigma} + U d_{\uparrow}^\dagger d_{\uparrow} d_{\downarrow}^\dagger d_{\downarrow} \\ & + V_h \sum_{\sigma} \left\{ d_{\sigma}^\dagger \psi_{\sigma}(\vec{R}_i) + \psi_{\sigma}^\dagger(\vec{R}_i) d_{\sigma} \right\}, \end{aligned} \quad (1)$$

$$\mathcal{H}_{tip} = \sum_{\vec{k}\sigma} (E_{\vec{k}} + eV) a_{\vec{k}\sigma}^\dagger a_{\vec{k}\sigma}, \quad (2)$$

$$\begin{aligned} \mathcal{H}_{tun} = & t_c \sum_{\sigma} \left\{ \psi_{\sigma}^\dagger(\vec{R}_s) A_{\sigma} + A_{\sigma}^\dagger \psi_{\sigma}(\vec{R}_s) \right\} \\ & + t_d \sum_{\sigma} \left\{ d_{\sigma}^\dagger A_{\sigma} + A_{\sigma}^\dagger d_{\sigma} \right\}. \end{aligned} \quad (3)$$

Here $c_{\vec{k}\sigma}^\dagger$ ($a_{\vec{k}\sigma}^\dagger$) creates a bulk (tip) conduction electron with wave number \vec{k} and spin projection σ , and d_{σ}^\dagger creates an atomic d electron with spin σ . The fermion operators $\psi_{\sigma}(\vec{r})$ and A_{σ} in Eqs. (1)–(3) are the local conduction electrons at point \vec{r} on the surface and at the edge of the STM tip, respectively. Explicitly,

$$\psi_{\sigma}(\vec{r}) = \sum_{\vec{k}} \varphi_{\vec{k}}(\vec{r}) c_{\vec{k}\sigma}, \quad (4)$$

$$A_{\sigma} = \sum_{\vec{k}} \chi_{\vec{k}} a_{\vec{k}\sigma}, \quad (5)$$

where $\varphi_{\vec{k}}(\vec{r})$ and $\chi_{\vec{k}}$ are the corresponding bulk and tip single-particle wave functions, evaluated at point \vec{r} on the surface and at the edge of the tip, respectively. The atomic energies $U + \epsilon_d$ and $-\epsilon_d$ are assumed to be positive and large, such that a local moment forms on the adatom.

For zero tunneling, $t_c, t_d = 0$, the local d moment undergoes Kondo screening below a characteristic temperature $T_K \propto \exp[-1/\rho_0 J]$, where ρ_0 is the local surface density of states at the Fermi level, and $J = 2V_h^2 [1/|\epsilon_d| + 1/(U + \epsilon_d)]$ is the effective exchange coupling between the d moment and the underlying $c_{\vec{k}\sigma}^\dagger$ conduction electrons. For nonzero tunneling and a finite

voltage bias, one is dealing in principle with a nonequilibrium state.^{7,8} However for a weak tunneling current, as is the case in the experiments of Ref. 1 and Ref. 2, the differential conductance essentially probes the zero-tunneling (equilibrium) Kondo resonance. To see this we note that, for weak tunneling, it is sufficient to evaluate the tunneling current from the substrate to the STM tip to second order in t_c and t_d . Using standard diagrammatic techniques one obtains

$$I(V) = \frac{2e}{\pi\hbar} \sum_{\sigma} \int_{-\infty}^{\infty} \rho_{A\sigma}(\epsilon - eV) \rho_{f\sigma}(\epsilon) [f(\epsilon - eV) - f(\epsilon)] d\epsilon, \quad (6)$$

where $f(\epsilon)$ is the Fermi-Dirac distribution function, and $\rho_{A\sigma}(\epsilon) = -\text{Im}G_{A\sigma}(\epsilon + i\eta)$ and $\rho_{f\sigma}(\epsilon) = -\text{Im}G_{f\sigma}(\epsilon + i\eta)$ are the zero-tunneling spectral functions corresponding to A_{σ} and

$$f_{\sigma} = t_c \psi_{\sigma}(\vec{R}_s) + t_d d_{\sigma}, \quad (7)$$

respectively. Here we have introduced the notation by which the arguments of $G_{A\sigma}$ and $G_{f\sigma}$ (and thus those of $\rho_{A\sigma}$ and $\rho_{f\sigma}$) are measured relative to their respective chemical potentials, i.e., $\mu_{tip} = eV$ and $\mu_{sub} = 0$.

All information of the Kondo effect in Eq. (6) is contained within the retarded $G_{f\sigma}$ propagator,

$$G_{f\sigma}(\epsilon + i\eta) = t_c^2 G_{\vec{R}_s, \vec{R}_s}(\epsilon + i\eta) + G_{\sigma}^d(\epsilon + i\eta) \times [t_d + t_c V_h G_{\vec{R}_s, \vec{R}_i}(\epsilon + i\eta)] [t_d + t_c V_h G_{\vec{R}_i, \vec{R}_s}(\epsilon + i\eta)], \quad (8)$$

which features the fully dressed impurity (d -electron) Green function in the absence of tunneling, $G_{\sigma}^d(\epsilon + i\eta)$, and the impurity-free surface Green function,

$$G_{\vec{r}_1, \vec{r}_2}(\epsilon + i\eta) = \sum_{\vec{k}} \frac{\varphi_{\vec{k}}(\vec{r}_1) \varphi_{\vec{k}}^*(\vec{r}_2)}{\epsilon - \epsilon_{\vec{k}} + i\eta}. \quad (9)$$

The differential conductance is given in turn by the derivative of Eq. (6) with respect to V . Assuming $\rho_{A\sigma}(\epsilon) = \rho_A$ is essentially energy independent on the scale of the voltage bias and the temperature, one obtains

$$G(V) = -\frac{2e^2}{\pi\hbar} \rho_A \int_{-\infty}^{\infty} \sum_{\sigma} \rho_{f\sigma}(\epsilon + eV) \frac{\partial f(\epsilon)}{\partial \epsilon} d\epsilon. \quad (10)$$

Equations (8)–(10) are a generalization of Fano's original analysis⁶ to the interacting case. They express the differential conductance in terms of the fully dressed impurity Green function, the impurity-free surface Green function, and the microscopic tunneling parameters of the model. The remainder of the paper is devoted to evaluation and analysis of these equations, starting with the Green functions $G_{\sigma}^d(\epsilon + i\eta)$ and $G_{\vec{r}_1, \vec{r}_2}(\epsilon + i\eta)$.

III. IMPURITY AND SURFACE GREEN FUNCTIONS

A. Impurity Green function

We have evaluated the impurity Green function in the limit $U \rightarrow \infty$, where double occupancy is forbidden on the magnetic adatom. Calculations were performed using the non-crossing approximation⁹ (NCA), which is a self-consistent perturbation theory about the atomic limit. This approach is known to provide a good quantitative description of the temperature range $T \gtrsim T_K$, and has the advantage of being capable of treating systems with realistically small Kondo temperatures. This is to be contrasted with Quantum Monte Carlo approaches, which can not go to very low temperatures. As a large- N theory, however, the NCA fails to recover Fermi-liquid behavior at low temperatures,⁹ and it overshoots the unitary limit for $T \lesssim T_K$ in the $N = 2$, nondegenerate case. To avoid these pathologies of the NCA, we restrict attention in this paper to the range $T \geq T_K$.

B. Surface Green function

Due to the local nature of the hybridization between the d and conduction electrons in Eq. (1), only the local conduction-electron density of states is relevant to the impurity Green function, $G_{\sigma}^d(\epsilon + i\eta)$. Conventionally, this allows one to parameterize the band by a single function for the density of states, often chosen for convenience to have a Lorentzian, box, or Gaussian form. In contrast, calculation of the differential conductance for $\vec{R}_s \neq \vec{R}_i$ requires detailed information of the band dispersion. In particular, a consistent theory for the energy and spatial dependence of $G(V)$ requires one to start from a microscopic description of the underlying conduction band.

As a generic model for the substrate conduction band, we consider a simple-cubic tight-binding Hamiltonian, with open boundary conditions at the surface. Setting the lattice spacing as our unit length, the lattice is described by the integer grid $\vec{r}_i = (x_i, y_i, z_i)$ with $z_i > 0$, such that the first (surface) monolayer corresponds to $z_i = 1$. In each of the x and y direction we take periodic boundary conditions, i.e., x_i and y_i are equivalent to $x_i + N$ and $y_i + N$, respectively. In the z direction we apply open boundary conditions, namely, $c_{\vec{r}_i, \sigma}$ (the conduction-electron annihilation operator at site \vec{r}_i) vanishes for $z_i = 0$ and $z_i = N$. The corresponding Hamiltonian reads

$$\mathcal{H}_{band} = t \sum_{\langle i, j \rangle, \sigma} \left\{ c_{\vec{r}_i, \sigma}^{\dagger} c_{\vec{r}_j, \sigma} + c_{\vec{r}_j, \sigma}^{\dagger} c_{\vec{r}_i, \sigma} \right\}, \quad (11)$$

where $\langle i, j \rangle$ denotes nearest-neighbor lattice sites. For $\mu_{sub} = 0$, the case considered here, the Hamiltonian of Eq. (11) describes a half-filled band.

The tight-binding Hamiltonian of Eq. (11) is diagonalized by converting to the single-particle basis

$$c_{\vec{k}\sigma} = \sqrt{\frac{2}{N^3}} \sum_i c_{\vec{r}_i\sigma} e^{-i(k_x x_i + k_y y_i)} \sin(k_z z_i). \quad (12)$$

Here \vec{k} takes the values $(2n_x, 2n_y, n_z)\pi/N$, with the integers $0 \leq n_x, n_y < N$ and $1 \leq n_z < N$. The corresponding single-particle energies take the form

$$\epsilon_{\vec{k}} = 2t \sum_{l=x,y,z} \cos(k_l). \quad (13)$$

Since the tight-binding wave functions $\varphi_{\vec{k}}(\vec{r})$ are confined to a discrete set of lattice sites, the Green function of Eq. (9) is meaningful only in the case where both \vec{r}_1 and \vec{r}_2 are lattice sites. Taking the thermodynamic limit, $N \rightarrow \infty$, one thus obtains

$$G_{\vec{r}_1, \vec{r}_2}(\epsilon + i\eta) = \frac{2}{\pi^3} \int_0^\pi dk_x \int_0^\pi dk_y \int_0^\pi dk_z \quad (14)$$

$$\times \cos[k_x(x_1 - x_2)] \cos[k_y(y_1 - y_2)] \frac{\sin(k_z z_1) \sin(k_z z_2)}{\epsilon - \epsilon_{\vec{k}} + i\eta},$$

from which the surface Green function follows by setting $z_1 = z_2 = 1$:

$$G_{lm}(\epsilon + i\eta) = \frac{2}{\pi^3} \int_0^\pi dk_x \int_0^\pi dk_y \int_0^\pi dk_z \quad (15)$$

$$\times \cos(k_x l) \cos(k_y m) \frac{\sin^2(k_z)}{\epsilon - \epsilon_{\vec{k}} + i\eta}.$$

Here and in the remainder of the paper we label the surface Green function by two integers: $l = x_1 - x_2$ and $m = y_1 - y_2$. We further note that $G_{lm}(\epsilon + i\eta)$ and $G_{ml}(\epsilon + i\eta)$ are identical by symmetry, and are only dependent upon the distances $|l|$ and $|m|$.

Equation (15) can be further simplified to just a single integration by exploiting the relation to the local tight-binding Green function for a two-dimensional, simple-cubic lattice:¹⁰

$$G_{2D}(\zeta) = \frac{2}{\pi\zeta} K[(4t/\zeta)^2]. \quad (16)$$

Here $K(\zeta)$ is the complete elliptic integral of the first kind, analytically continued to the upper and lower half planes.¹¹ Specifically, the local surface Green function, G_{00} , is conveniently expressed as

$$G_{00}(\epsilon + i\eta) = \frac{2}{\pi} \int_0^\pi dk \sin^2(k) G_{2D}[\epsilon - 2t \cos(k) + i\eta], \quad (17)$$

with analogous expressions for the first few nonlocal Green functions (see Appendix A).

Figure 2 displays the first four surface Green functions. Both the real and imaginary parts of $G_{lm}(\epsilon + i\eta)$ decay

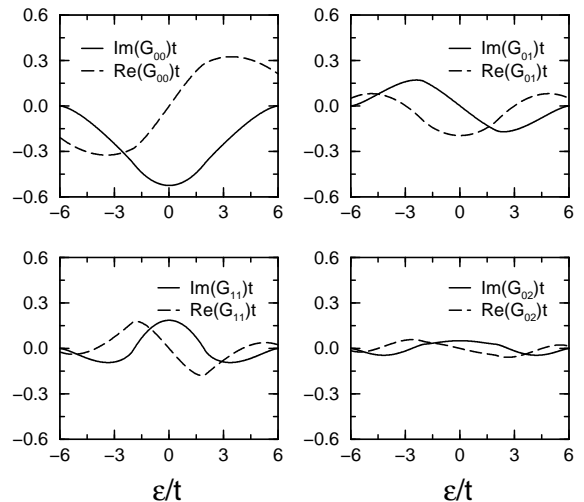


FIG. 2. Real and imaginary parts of the tight-binding surface Green function $G_{lm}(\epsilon + i\eta)$, for different values of (l, m) .

as a function of $\sqrt{l^2 + m^2}$, alternating between even and odd functions of energy. For even (odd) $|l| + |m|$, the real part of $G_{lm}(\epsilon + i\eta)$ is odd (even) in energy, while the imaginary part is even (odd). As a result, $G_{lm}(0 + i\eta)$ is purely imaginary when $|l| + |m|$ is even, and purely real when $|l| + |m|$ is odd. This has a profound effect on the spatial dependence of the low-voltage differential conductance for this model, as a purely real $G_{lm}(0 + i\eta)$ gives rise to resonant enhancement of the differential conductance for $\vec{R}_s - \vec{R}_i = (l, m, 0)$. By contrast, an imaginary $G_{lm}(0 + i\eta)$ can result both in an antiresonance or an asymmetric Fano resonance, depending on details of the tunneling matrix elements t_c and t_d . We shall return to this point in great detail below. Finally, we note that the imaginary part of $G_{lm}(0 + i\eta)$ is nonzero only in the range $-6t < \epsilon < 6t$, and that the van-Hove singularities at $\epsilon = \pm 2t$ are considerably smoother at the surface than deep inside the bulk.

IV. RESULTS FOR POINT TUNNELING

We have evaluated the differential conductance according to Eqs. (8)–(10), within the tight-binding model of Eq. (11) for the underlying conduction band. $\psi_\sigma^\dagger(\vec{R}_i)$ was identified in this picture with the creation of an electron at the lattice site $\vec{R}_i = (0, 0, 1)$. The local density of states used in computing the impurity Green function was taken accordingly to be $\rho(\epsilon) = -\frac{1}{\pi} \text{Im} \{G_{00}(\epsilon + i\eta)\}$, where G_{00} is given by Eq. (17). The corresponding density of states at the Fermi level is equal to $\rho_0 = \rho(0) = 0.525/t$. Focusing on the case where the STM tip is positioned directly above the lattice site $\vec{R}_s = (l, m, 1)$, each of the surface Green functions $G_{\vec{R}_s, \vec{R}_i}(\epsilon + i\eta)$ and $G_{\vec{R}_i, \vec{R}_s}(\epsilon + i\eta)$ in Eq. (8) was identified with $G_{lm}(\epsilon + i\eta)$.

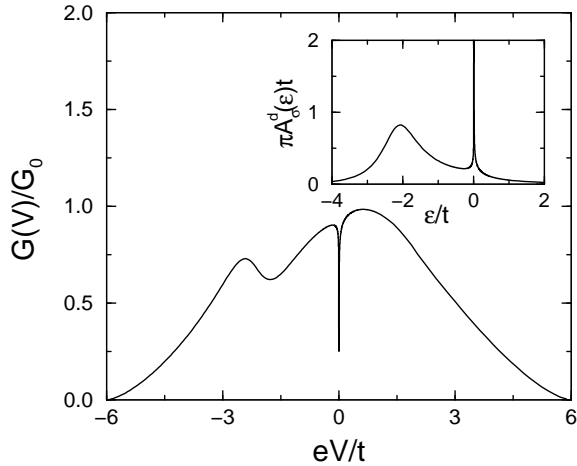


FIG. 3. The differential conductance, $G(V)$, as a function of voltage, for an STM tip placed directly above the magnetic adatom. Here $T = T_K$, $t_d = 0$, and $G_0 = 4e^2 t_c^2 \rho_0 \rho_A / \hbar$. The impurity model parameters are $\epsilon_d/t = -1.67$, $\Gamma/t = 0.4$, and $U = \infty$, corresponding to a Kondo temperature of $T_K/t = 10^{-3}$. The impurity Green function, whose spectral part $A_\sigma^d(\epsilon) = -(1/\pi)\text{Im}\{G_\sigma^d(\epsilon + i\eta)\}$ is plotted in the inset, was computed using the NCA. In addition to the standard broad feature near the d level, a sharp antiresonance is seen in $G(V)$ at zero bias, corresponding to the Abrikosov-Suhl resonance in the impurity spectral function.

A. Tip placed above the magnetic adatom

We begin with an STM tip positioned directly above the magnetic adatom. As the temperature is lowered down to T_K , a sharp resonant structure develops in the differential conductance at zero bias, in addition to the standard broad feature near the d level. This is demonstrated Fig. 3 for $T = T_K$ and $t_d = 0$. The sharp antiresonance seen at zero bias in this case directly corresponds to the Abrikosov-Suhl resonance in the impurity spectral function, which is plotted for comparison in the inset of Fig. 3. Here and throughout the paper, the impurity Green function was calculated within the NCA, using the impurity model parameters $\epsilon_d/t = -1.67$, $\Gamma/t \equiv \pi\rho_0 V_h^2/t = 0.4$, and $U = \infty$.¹² The corresponding Kondo temperature, $T_K/t = 10^{-3}$, was defined as the temperature at which the “resistivity” integral,¹³

$$R(T) = \left[\int_{-\infty}^{\infty} \frac{1}{\text{Im}\{G_\sigma^d(\epsilon + i\eta)\}} \frac{\partial f(\epsilon)}{\partial \epsilon} d\epsilon \right]^{-1}, \quad (18)$$

reduces to 50% of its zero-temperature limit. This definition of T_K agrees to within a factor of order unity with the half-width of the Abrikosov-Suhl resonance in the impurity spectral function.

Focusing hereafter on the low-voltage resonant structure, Fig. 4 depicts the resonance’s dependence on $q_0 = t_d/\pi\rho_0 t_c V_h$, which plays the role of Fano’s interference parameter q in this case. Here $G_0 = 4e^2 t_c^2 \rho_0 \rho_A / \hbar$ is the

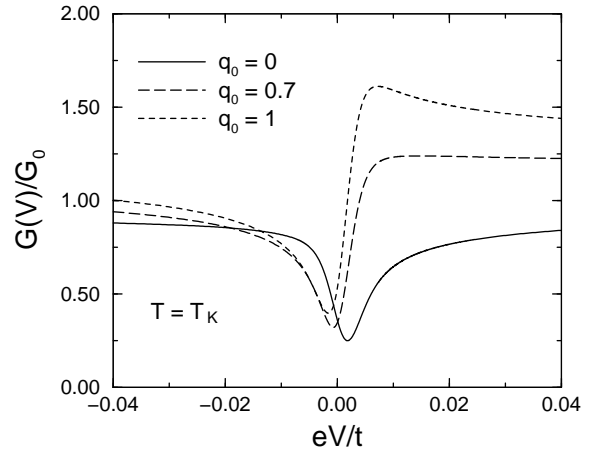


FIG. 4. The low-voltage differential conductance for an STM tip placed directly above the magnetic adatom. Here $T = T_K$ and $q_0 = t_d/\pi\rho_0 t_c V_h$, with all other model parameters as in Fig. 3. With increasing $|q_0|$, $G(V)$ evolves from an antiresonance for $|q_0| \ll 1$, to an asymmetric Fano resonance for intermediate $|q_0|$, to a full resonance for $|q_0| \gg 1$ (not shown).

zero-temperature conductance in the absence of an impurity. With increasing $|q_0|$, the low-voltage differential conductance evolves in Fig. 4 from an antiresonance for $|q_0| \ll 1$, to an asymmetric Fano resonance for intermediate $|q_0|$, to a full resonance for $|q_0| \gg 1$, much in the same way as in the noninteracting case. The antiresonance for $q_0 = 0$ resembles that for a Ce adatom on Ag(111),¹ supporting the interpretation of Li *et al.* that the observed lineshape stems from Kondo screening of the Ce moment with only weak direct coupling between the tip and the adatom. The $q_0 = 1$ curve is similar in turn to the Fano resonance observed by Madhavan *et al.* for a Co adatom on Au(111),² while larger values of q_0 display too shallow a dip and too high a peak as compared to the data of Ref. 2.

Figure 5 shows the temperature dependence of $G(V)$, for the two representative values of $q_0 = 0$ and $q_0 = 0.7$. The main effect of a temperature is to broaden and smear the resonant structure in $G(V)$, whose width grows according to T for $T > T_K$. Notice the significant reduction in the overall resonance height by the time $T/T_K \sim 10$. This strong temperature dependence of the differential conductance has two contributions: (i) A rapid decrease in the Abrikosov-Suhl resonance in the impurity spectral function with increasing temperature, and (ii) Further smearing of the impurity Green function due to the convolution with the derivative of the Fermi-Dirac function in Eq. (10). The fact that the well-developed features in Refs. 1 and 2 have widths that are notably larger than T is thus a clear indication that $T < T_K$ in both experiments.

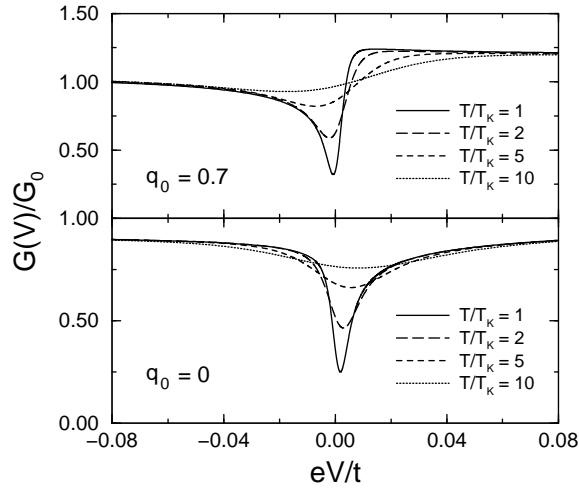


FIG. 5. Temperature dependence of $G(V)$, for an STM tip placed directly above the magnetic adatom. Here $q_0 = 0$ and $q_0 = 0.7$ in the lower and upper graphs, respectively. All other model parameters as in Fig. 3.

B. Spatial dependence of the differential conductance

As stated above, the novel aspect of STM spectroscopy of the Kondo effect is the ability to spatially resolve the electronic structure around the magnetic adatom. In Fig. 6 we have plotted the low-voltage differential conductance as a function of (l, m) , for the idealized case where the STM tip is placed directly above the lattice site $\vec{R}_s = (l, m, 1)$. Here each set of curves corresponds to a different fixed value of $q_0 = t_d/\pi\rho_0 t_c V_h$, which no longer corresponds for $\vec{R}_s \neq \vec{R}_i$ to Fano's interference parameter q . The latter also depends on the real and imaginary parts of $G_{\vec{R}_s, \vec{R}_i}(0 + i\eta)$, as discussed below. Physically one should recall, though, that $q_0 \propto t_d$ decays to zero with increasing distance from the magnetic adatom, hence $G(V)$ always tends to the $q_0 = 0$ curve as the lateral distance from the adatom is increased.

Fixing the value of q_0 for the time being and increasing the lateral distance from the magnetic adatom, the low-bias differential conductance approaches the asymptotic curve

$$G(V) = G_0 \left[1 + \Gamma q_0^2 \int_{-\infty}^{\infty} \text{Im}\{G_{\sigma}^d(\epsilon + i\eta)\} \frac{\partial f(\epsilon)}{\partial \epsilon} d\epsilon \right]. \quad (19)$$

This result stems from the decaying nature of $G_{lm}(0+i\eta)$, along with the fact that $G_{00}(\epsilon + i\eta) = -i\pi\rho_0$ is approximately constant on the scale of the voltage bias and the temperature. As seen in Fig. 6, Eq. (19) is approached at a lateral distance of about two lattice spacings from the magnetic adatom. For larger distances the resonance height is basically proportional to the residual coupling to the magnetic adatom squared. Specifically, there are

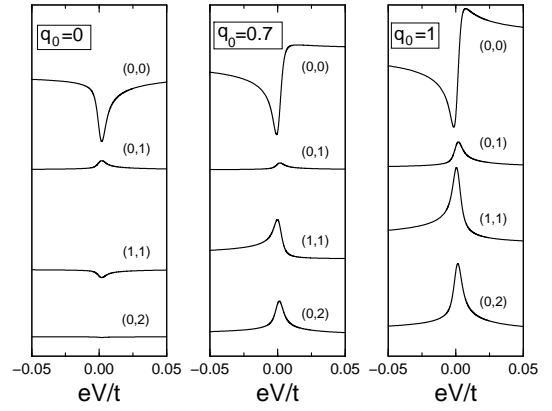


FIG. 6. Spatial dependence of the low-voltage differential conductance, $G(V)$, for $T = T_K$ and different values of $q_0 = t_d/\pi\rho_0 t_c V_h$. All impurity model parameters are as in Fig. 3. The individual curves are offset by one unit each, according to the lateral distance from the impurity site.

no visible traces of the Kondo resonance for $q_0 = 0$ when the tip and the adatom are two lattice spacings apart [the curve $(l, m) = (0, 2)$ in Fig. 6]. Such a limited spatial extent of the Kondo resonance in $G(V)$ is consistent with the one seen experimentally for Co on Au(111),² indicating that q_0 is effectively zero in the experiment above a lateral distance of about 10\AA . Indeed, the low-bias resonant structure is also mostly gone by lateral distance of 10\AA for Ce on Ag(111),¹ even though the Ag(111) surface state at -70meV does not fully set in before a distance of about 40\AA .

The resonant enhancement of $G(V)$ at a lateral distance of one lattice spacing, which occurs for any value of q_0 , is not seen in the experiment. This feature of the calculated differential conductance is traced back to the fact that $G_{01}(0 + i\eta)$ is purely real for our tight-binding model, resulting in a differential conductance $G(V)$ that is once again given by Eq. (19), but with

$$q_0 \rightarrow q_0 + \frac{1}{\pi\rho_0} \text{Re}\{G_{01}(0 + i\eta)\} = q_0 - 0.372 \quad (20)$$

[see Eqs. (8) and (10)]. Thus, irrespective of the actual q_0 that applies to a lateral distance of one lattice spacing in the experiment of Madhavan *et al.*, our present model fails to recover the dip-like structure seen experimentally at such a distance for Co on Au(111).²

That $G_{01}(0 + i\eta)$ is purely real is a generic feature of half-filled nearest-neighbor tight-binding models on bipartite lattices. It is lost, however, when the system is away from half filling, or upon inclusion of a next-nearest-neighbor hopping term. This suggests that the dip-like structure seen experimentally up to a distance of $\sim 10\text{\AA}$ from the Co adatom² is due to a qualitative difference in the underlying surface Green function for Au(111). Indeed, the (111) surface of gold is known to have a herringbone reconstruction with regions of fcc and hcp ordering,¹⁴ which differs from the simple-cubic structure

considered here. This may support the interpretation of a qualitative difference in the underlying surface Green function.

It should be noted, though, that such an interpretation for Au(111) demands that $\text{Im}\{G_{\vec{R}_i, \vec{R}_s}(0 + i\eta)\}$ is never small compared to $\pi\rho_0q_0 + \text{Re}\{G_{\vec{R}_i, \vec{R}_s}(0 + i\eta)\}$ in the relevant range in $\vec{R}_s - \vec{R}_i$. In particular, this rules out any oscillatory behavior of $\text{Im}\{G_{\vec{R}_i, \vec{R}_s}(0 + i\eta)\}$ as a function of $\vec{R}_s - \vec{R}_i$ in this range. A brief examination of Fig. 2 reveals that this condition is actually quite restrictive, at least for the tight-binding model of Eq. (11): Only in a narrow window of band fillings is $\text{Im}\{G_{lm}(0 + i\eta)\}$ consistently negative for all $|l| + |m| \leq 2$. We thus conclude that the spatial dependence measured by Madhavan *et al.* is certainly not generic, but depends on details of the underlying band.

V. FINITE SPATIAL EXTENT OF THE TUNNELING MATRIX ELEMENT

Thus far we have considered an idealized point tunneling between the STM tip and the substrate conduction electrons at point \vec{R}_s . In practice, however, the tunneling matrix element has a finite spatial extent about \vec{R}_s , which is reflected in the different lineshapes that are observed when the tip is removed from the Co adatom in opposite directions.² On the level of the model, a spatially extended tunneling matrix element is accounted for by replacing $\psi_\sigma(\vec{R}_s)$ in the first term of Eq. (3) with a weighed sum over the conduction-electron degrees of freedom around \vec{R}_s :

$$\psi_\sigma(\vec{R}_s) \rightarrow \sum_{\vec{r}} w_{\vec{r}} \psi_\sigma(\vec{R}_s + \vec{r}). \quad (21)$$

Here we use the convention

$$\sum_{\vec{r}} |w_{\vec{r}}|^2 = 1, \quad (22)$$

which fixes the separation of the local tunneling matrix element at each \vec{r} into $t_{\vec{r}} = t_c w_{\vec{r}}$. For the tight-binding model of Eq. (11), the sum over \vec{r} in Eq. (21) extends over those lattice sites close to the STM tip.

Upon substituting Eq. (21) into the tunneling Hamiltonian of Eq. (3), the differential conductance remains given by Eqs. (8)–(10), but with the following modifications to Eq. (8):

$$G_{\vec{R}_s, \vec{R}_s} \rightarrow \sum_{\vec{r}, \vec{r}'} w_{\vec{r}} w_{\vec{r}'}^* G_{\vec{R}_s + \vec{r}, \vec{R}_s + \vec{r}'}, \quad (23a)$$

$$G_{\vec{R}_s, \vec{R}_i} \rightarrow \sum_{\vec{r}} w_{\vec{r}} G_{\vec{R}_s + \vec{r}, \vec{R}_i}, \quad (23b)$$

$$G_{\vec{R}_i, \vec{R}_s} \rightarrow \sum_{\vec{r}} w_{\vec{r}}^* G_{\vec{R}_i, \vec{R}_s + \vec{r}}. \quad (23c)$$

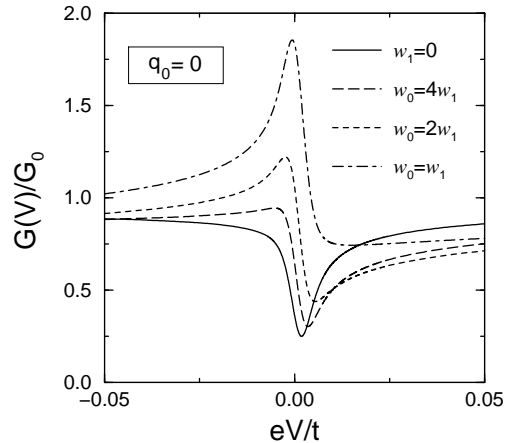


FIG. 7. The differential conductance, $G(V)/G_0$, as a function of w_1/w_0 , for $T = T_K$, $q_0 = 0$, and an STM tip placed directly above the magnetic adatom. Here both w_0 and w_1 are assumed to be real and positive. Note that G_0 itself varies as a function of w_1/w_0 [see Eq. (24)], taking the values $G_0\hbar/4e^2t_c^2\rho_0\rho_A = 1, 0.838, 0.598$, and 0.356 for $w_1/w_0 = 0, 0.25, 0.5$, and 1 , respectively. All impurity model parameters are as in Fig. 3. As the ratio w_1/w_0 is increased from zero to one, $G(V)$ evolves from an antiresonance to a resonance, corresponding to an increase in the effective interference parameter q [see Eq. (27) and accompanying text].

Accordingly, the zero-temperature conductance in the absence of an adatom is equal to

$$G_0 = -\frac{4e^2t_c^2}{\pi\hbar}\rho_A \text{Im} \left\{ \sum_{\vec{r}, \vec{r}'} w_{\vec{r}} w_{\vec{r}'}^* G_{\vec{R}_s + \vec{r}, \vec{R}_s + \vec{r}'}(0 + i\eta) \right\}, \quad (24)$$

which properly reduces to $G_0 = 4e^2t_c^2\rho_0\rho_A/\hbar$ in the limit of point tunneling.

To examine the effect of a finite spatial extent in the tunneling matrix element, we go back to the tight-binding model of Eq. (11), and to the case where the tip is placed directly above the magnetic adatom, i.e., $\vec{R}_s = (0, 0, 1)$. In addition to tunneling between the tip and the lattice point \vec{R}_s , we introduce a nonzero tunneling matrix element to each of the four surface nearest-neighbors of \vec{R}_s . Restricting attention to the isotropic case, one is left with two different $w_{\vec{r}}$ parameters: w_0 for the tunneling matrix element to the lattice point \vec{R}_s , and w_1 for the tunneling matrix element to each of its four surface nearest neighbors. The normalization condition, Eq. (22), then reads

$$|w_1| = \frac{1}{2} \sqrt{1 - |w_0|^2}. \quad (25)$$

Figures 7 and 8 depict the evolution of the low-voltage differential conductance $G(V)/G_0$ as a function of w_1/w_0 , for the two representative values of $q_0 = 0$ and $q_0 = 0.7$. Here we have focused for simplicity on the

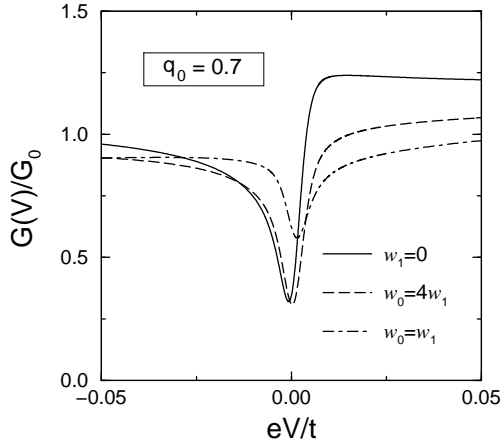


FIG. 8. Same as Fig. 7, but for $q_0 = 0.7$. As the ratio w_1/w_0 is increased from zero to one, $G(V)$ evolves from an asymmetric Fano resonance to an antiresonance, corresponding to a decrease in the effective interference parameter q [see Eq. (27) and accompanying text].

case where w_0 and w_1 are both real and positive, yet the qualitative picture does not depend on this choice. The dramatic effect that a nonzero w_1 has on the differential conductance in this case can be understood within Fano's interference picture. Substituting Eqs. (23) into Eq. (8) and taking w_0 and w_1 to be real, the effective interference parameter *à la* Fano is given for $\vec{R}_s = \vec{R}_i$ by minus the ratio of the real and imaginary parts of

$$t_d + t_c V_h [w_0 G_{00}(0 + i\eta) + 4w_1 G_{01}(0 + i\eta)]. \quad (26)$$

Here Eq. (26) corresponds to the resulting expression in each of the square brackets of Eq. (8). Using $G_{00}(0 + i\eta) = -i\pi\rho_0$ and $G_{01}(0 + i\eta) = -0.372\pi\rho_0$, as is appropriate for the model of Eq. (11), one obtains

$$q = (q_0 - 1.49w_1)/w_0. \quad (27)$$

For $q_0 = 0$, Eq. (27) reduces to $-1.49(w_1/w_0)$, which varies from $q = 0$ to $q = -1.49$ in going from $w_1 = 0$ to $w_1 = w_0$. This strong change in q produces the transition from an antiresonance to a resonance in the differential conductance of Fig. 7. Similarly for $q_0 = 0.7$, Eq. (27) varies from $q = 0.7$ to $q = 0.075$ in going from $w_0 = 1$ to $w_0 = w_1$, which causes the transition from an asymmetric Fano resonance to an antiresonance in Fig. 8.

Repeating the same argumentation for the case where \vec{R}_s and \vec{R}_i are one lattice spacing apart, i.e., $\vec{R}_s = (\pm 1, 0, 1)$ or $\vec{R}_s = (0, \pm 1, 1)$, Eq. (26) is modified to

$$t_d + t_c V_h [w_0 G_{01} + w_1 G_{00} + 2w_1 G_{11} + w_1 G_{02}], \quad (28)$$

with all Green functions evaluated at zero frequency. Using $G_{11}(0 + i\eta) = 0.354i\pi\rho_0$ and $G_{02}(0 + i\eta) = 0.097i\pi\rho_0$ one obtains

$$q = (5.1q_0 - 1.9w_0)/w_1, \quad (29)$$

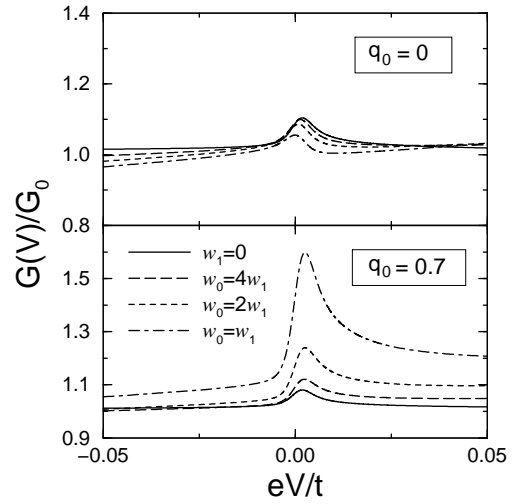


FIG. 9. The differential conductance, $G(V)/G_0$, as a function of w_1/w_0 , for an STM tip one lattice spacing removed from the magnetic adatom [i.e., $\vec{R}_s = (\pm 1, 0, 1)$ or $(0, \pm 1, 1)$]. As in Fig. 7, w_0 and w_1 are assumed to be real and positive, with all impurity model parameters the same as in Fig. 3. For both $q_0 = 0$ and $q_0 = 0.7$, the differential conductance continues to feature a resonance for all $0 \leq w_1/w_0 \leq 1$.

which is large in magnitude throughout the range $0 < w_1 \leq w_0$, for both $q_0 = 0$ and $q_0 = 0.7$. Given the large value of $|q|$, one expects the differential conductance to continue to show a resonance for both values of q_0 and all $0 \leq w_1/w_0 \leq 1$, which is precisely what is seen in Fig. 9.

Thus, while the inclusion of nonlocal tunneling between the STM tip and the underlying substrate conduction electrons obviously increases the parametric dependence of q , it does not necessarily assist in producing a dip in the low-voltage differential conductance when the tip and the adatom are one lattice spacing apart.

VI. DISCUSSION

We begin our discussion with the case of an STM tip placed directly above the magnetic adatom, depicted in Figs. 3–5 and Figs. 7–8. Similar to the noninteracting case, the shape of the Kondo resonance in the low-temperature, low-voltage differential conductance is governed by a single interference parameter q , which depends both on the ratios of the tunneling matrix elements and on details of the impurity-free surface Green function. Specifically, in Fig. 4 q is equal to $q_0 = t_d/\pi\rho_0 t_c V_h$, whereas in Figs. 7–8 it is modified according to Eq. (27). The effect of a temperature is to rapidly broaden and smear the Kondo resonance in $G(V)$, whose width grows according to T for $T > T_K$. This behavior stems both from the standard convolution with the derivative of the Fermi-Dirac distribution function in Eq. (10), and from the rapid decrease in the Abrikosov-Suhl resonance with

increasing temperature. Indeed, the qualitative difference in the low-temperature, low-voltage differential conductance for a magnetic adatom as compared to that of a conventional noninteracting resonance is in the strong energy and temperature dependence of the impurity self-energy, whose real and imaginary parts cannot be regarded a constant.

Experimentally, the antiresonance observed for Ce on Ag(111)¹ is similar to the $q_0 = 0$ curve in Fig. 4. Assuming point tunneling between the tip and the underlying conduction electrons, this supports the interpretation of weak direct tunneling between the tip and the Ce adatom,¹ which requires at the same time that $G_{\vec{R}_i, \vec{R}_i}(0 + i\eta)$ is mostly imaginary. While plausible, this scenario is certainly not exclusive, as there are various other ways to obtain $q \approx 0$ without resorting to a negligible coupling to the adatom. For example, the curve $w_0 = w_1$ in Fig. 8 (corresponding to a spatially extended tunneling) is also characterized by $|q| \ll 1$, although $q_0 = 0.7$ is by no means small. Likewise, while the similarity between the $q_0 = 1$ curve in Fig. 4 and the Fano resonance for Co on Au(111)² is suggestive of comparable contributions from the tunneling to the adatom and to the underlying conduction electrons, one cannot rule out other combinations for which $q_0 \approx 0$. For example, setting $q_0 \approx 0$ and $w_0/w_1 \approx -1.5$ in Eq. (27) also results in $q \approx 1$. On the other hand, the fact that the well-developed features in Refs. 1 and 2 have characteristic widths that are considerably larger than the temperature is a clear indication that $T < T_K$ in both experiments.

More detailed information about the underlying electronic structure is contained in the spatial variation of the differential conductance, as measured, for example, in Ref. 2 for a Co adatom on Au(111). Here, although we have considered a particular tight-binding model for the impurity-free surface, there are some qualitative statements we can make with regard to the experiment. Primarily, as seen in Fig. 6, the indirect interference with the magnetic adatom, i.e., that due to the tunneling between the STM tip and the underlying conduction electrons, is suppressed above a lateral distance of about two lattice spacings from the adatom. Hence the characteristic range for the indirect interference with the adatom is of the order of two lattice spacings. While this range may certainly depend both on details of the underlying band and on the presence of nonlocal tunneling between the tip and the substrate conduction electrons, we expect a qualitatively similar result for other microscopic models. From the limited spatial extent of the Kondo resonance for Ce on Ag(111)¹ and Co on Au(111)² we thus conclude that q_0 is effectively zero above a lateral distance of about 10\AA in these experiments.

Our calculations further indicate that the spatial dependence of the differential conductance as measured for Co on Au(111) is not generic, but intimately depends on the microscopic details of Au(111). Indeed, while Madhavan *et al.* observe a dip-like structure that persists up to a lateral distance of $\sim 10\text{\AA}$ from the adatom,² we typically

find a resonance at a distance of one lattice spacing. In Fig. 6, where point tunneling is assumed, this resonance occurs for any value of q_0 , which is a special feature of the half-filled nearest-neighbor tight-binding model used. One may anticipate, though, a similar resonance within a range of one lattice spacing for other lattice models at half filling, since $G_{\vec{R}_s, \vec{R}_i}(0 + i\eta)$ is expected to oscillate on a length scale of one lattice spacing. We emphasize, however, that the spatial dependence measured by Madhavan *et al.* remains quite restrictive for the Hamiltonian of Eq. (11) both away from half filling and in the case of nonlocal tunneling between the tip and the substrate conduction electrons.

The particular tight-binding model used in this paper clearly limits the application of our results to the experiments. To make direct contact with the experimental data it is necessary to employ realistic Green functions for the (111) surfaces of silver and gold, which may be obtained, for example, from *ab-initio* calculations. It would be interesting to see if the combination of *ab-initio* calculations for the (111) surface of gold with NCA calculations for the many-body Kondo resonance can reproduce the particular spatial dependence of the differential conductance as seen for Co on Au(111).

Another interesting issue is the magnetic-field dependence of the low-temperature, low-voltage differential conductance. With increasing magnetic field, the Abrikosov-Suhl resonance is first split for a moderate magnetic field, $H \sim T_K$, before a large magnetic field suppresses the Kondo effect altogether. A similar pattern is expected for the Kondo resonance in the differential conductance. Unfortunately, treatment of a finite magnetic field within the NCA is hampered by the NCA pathology,⁹ hence a different approach is required. One possibility might be Quantum Monte Carlo simulations in combination with the Maximum Entropy method for analytic continuation,¹⁶ although such an approach is restricted in treating realistically small Kondo temperatures.

Finally, in this paper we have focused on the case of an individual magnetic adatom; however, using the STM tip to atomically manipulate individual adatoms into forming small clusters, it might be possible to address the subtle interplay between the Kondo effect and magnetic correlations among the different adatoms. Most notably, the competition between the Kondo effect and antiferromagnetic locking in the case of two close-by adatoms.¹⁷ A first study of a Co dimer on Au(111) along these lines was recently reported in Ref. 18. As detailed in Appendix C, our formulation of the tunneling current is naturally extended to the case of multiple magnetic adatoms. Specifically, the single d -electron Green function entering Eq. (8) is replaced by a matrix propagator, corresponding to all possible propagations within the adatom cluster. In this manner, one can analyze complicated multiple-adatom configurations in terms of the intra-site and inter-site d Green functions.

It is our hope that the approach developed in this paper will prove useful in analyzing future STM measurements of magnetic adatoms on metallic surfaces.

ACKNOWLEDGEMENTS

A. S. is grateful to Wilfrid Aulbur, Frithjof Anders, Amit Chattopadhyay, Daniel Cox, and John Wilkins for stimulating discussions. S. H. was supported in part by NSF grant DMR9357474, the NHMFL, and the Research Corporation.

APPENDIX A: SIMPLIFIED EXPRESSIONS FOR THE FIRST THREE NONLOCAL SURFACE GREEN FUNCTIONS

In this appendix, we provide simplified expressions for the nonlocal surface Green functions G_{01} , G_{11} , and G_{02} , involving just a single integration. These expressions are analogous to Eq. (17) for G_{00} .

Denoting for convenience $z = \epsilon + i\eta$ and $\zeta_k = z - 2t \cos(k)$, the nonlocal Green functions are expressed as

$$G_{lm}(z) = \int_0^\pi G_{2D}(\zeta_k) F_{lm}(z, k) \frac{dk}{\pi}, \quad (\text{A1})$$

with

$$F_{01}(z, k) = \cos(k) - \cos(2k) \frac{\zeta_k}{4t}, \quad (\text{A2})$$

$$F_{11}(z, k) = \cos(k) \left\{ \left(2 - \frac{z^2}{6t^2} \right) \frac{\zeta_k}{4t} + \frac{z}{3t} \right\} + \cos(2k) \frac{z\zeta_k}{12t^2}, \quad (\text{A3})$$

and

$$F_{02}(z, k) = \cos(k) \left\{ \left(\frac{z^2}{3t^2} - 1 \right) \frac{\zeta_k}{4t} - \frac{2z}{3t} \right\} + \cos(2k) \left\{ 2 - \frac{5z\zeta_k}{12t^2} \right\} + \cos(3k) \frac{\zeta_k}{4t}. \quad (\text{A4})$$

Similar expressions, but with modified $F_{lm}(z, k)$, apply also to $G_{lm}(z)$ with larger values of $|l| + |m|$.

APPENDIX B: COMPARISON WITH PREVIOUS WORK

It is instructive to compare the present theory of point tunneling between the STM tip and the substrate conduction electrons, Eqs. (8)–(10), with the analyses of

Refs. 1 and 2, which focused on the case where $\vec{R}_i = \vec{R}_s$. In Ref. 1, Li *et al.* considered the case of zero direct tunneling between the tip and adatom, corresponding to $q = 0$ in Fano's notation. The antiresonance that develops in $G(V)$ in this case was approximated by the inverted NCA lineshape of the impurity spectral function, computed within a degenerate Anderson model that accounts for the full $4f$ degeneracy in Ce. The depth of the antiresonance was left as a fitting parameter.

As evident from Eqs. (8)–(10) with $\vec{R}_i = \vec{R}_s$, the above relation between the impurity contribution to the differential conductance and the impurity spectral function is exact in the limit $T \rightarrow 0$, provided $G_{00}(\epsilon + i\eta) = -i\pi\rho_0$ is essentially constant for $|\epsilon|$ on the scale of T_K . This relation loses accuracy, though, for $T > T_K$, when the convolution with the derivative of the Fermi-Dirac function in Eq. (10) increasingly smears the lineshape of the impurity spectral function.

Contrary to Li *et al.*, who restricted attention to $q = 0$, Madhavan *et al.* considered the full range in q . To this end, Fano's expression for the differential conductance was generalized according to²

$$G(V) = G_0 \frac{(q + eV')^2}{1 + (eV')^2}, \quad (\text{B1})$$

$$eV' = \frac{eV - \epsilon_d - \text{Re} \{ \Sigma_\sigma^d(eV + i\eta) \}}{\text{Im} \{ \Sigma_\sigma^d(eV + i\eta) \}}, \quad (\text{B2})$$

where $\Sigma_\sigma^d(\epsilon + i\eta)$ is the full d -electron self-energy, including both the on-site repulsion U and the hybridization to the conduction band, V_h . The d self-energy was approximated in turn by a form corresponding to a Lorentzian Abrikosov-Suhl resonance, with a half-width T_K and a peak position that was left as a fitting parameter.

Comparison with Eqs. (8)–(10) for $\vec{R}_i = \vec{R}_s$ reveals that Eqs. (B1)–(B2) are correct in the limit $T \rightarrow 0$, provided $\text{Im} \{ \Sigma_\sigma^d(\epsilon + i\eta) \} = -\Gamma$. The latter equality is exact for $T = 0$ and $\epsilon = 0$,¹⁵ and is a reasonable approximation for $T < T_K$ and $|\epsilon| \lesssim T_K$. This approach, however, breaks down for $T > T_K$, both due to the inapplicability of the assumed form of $\Sigma_\sigma^d(\epsilon + i\eta)$, and because of the convolution with the derivative of the Fermi-Dirac function in Eq. (10) which smears the underlying structure of $G_{f\sigma}(\epsilon + i\eta)$. Hence, similar to the analysis of Li *et al.*, this approach is restricted to the low-temperature regime. By contrast, Eqs. (8)–(10) are valid for any temperature T and any $\vec{R}_s \neq \vec{R}_i$, and are easily amendable [using Eqs. (23)] to the case of nonlocal tunneling between the STM tip and the substrate conduction electrons.

APPENDIX C: SEVERAL MAGNETIC ADATOMS

In this appendix, we generalize our formulation of the tunneling current to the case of several magnetic adatoms

deposited on top of the metallic surface. Specifically, we consider a cluster of m close-by adatoms positioned at points \vec{R}_j ($j = 1, \dots, m$), each with its own hybridization matrix element, V_{hj} , and its own tunneling matrix element, t_j . The different adatoms need not be identical, and can generally have different d -level energies and different on-site Coulomb repulsions (denoted by ϵ_j and U_j , respectively). The Hamiltonian of the system has the form $\mathcal{H} = \mathcal{H}_{sub} + \mathcal{H}_{tip} + \mathcal{H}_{tun}$, where \mathcal{H}_{tip} is described by Eq. (2), and \mathcal{H}_{sub} and \mathcal{H}_{tun} are given by

$$\mathcal{H}_{sub} = \sum_{\vec{k}\sigma} \epsilon_{\vec{k}} c_{\vec{k}\sigma}^\dagger c_{\vec{k}\sigma} + \sum_j \left\{ \epsilon_j \sum_{\sigma} n_{j\sigma}^d + U_j n_{j\uparrow}^d n_{j\downarrow}^d \right\} + \sum_{j,\sigma} V_{hj} \left\{ d_{j\sigma}^\dagger \psi_{\sigma}(\vec{R}_j) + \psi_{\sigma}^\dagger(\vec{R}_j) d_{j\sigma} \right\}, \quad (\text{C1})$$

$$\mathcal{H}_{tun} = t_c \sum_{\sigma} \left\{ \psi_{\sigma}^\dagger(\vec{R}_s) A_{\sigma} + A_{\sigma}^\dagger \psi_{\sigma}(\vec{R}_s) \right\} + \sum_j t_j \sum_{\sigma} \left\{ d_{j\sigma}^\dagger A_{\sigma} + A_{\sigma}^\dagger d_{j\sigma} \right\}. \quad (\text{C2})$$

Here $d_{j\sigma}^\dagger$ creates an atomic d electron with spin σ on the j -th adatom, and $n_{j\sigma}^d = d_{j\sigma}^\dagger d_{j\sigma}$ is the corresponding number operator. All other notations are the same as in Eqs. (1)–(3).

Evaluating the tunneling current from the substrate to the tip to second order in t_c and t_j , one obtains an expression identical to that of Eq. (6), with the sole modification that $\rho_{f\sigma}(\epsilon) = -\text{Im}G_{f\sigma}(\epsilon + i\eta)$ represents now the zero-tunneling spectral function corresponding to

$$f_{\sigma} = t_c \psi_{\sigma}(\vec{R}_s) + \sum_j t_j d_{j\sigma}. \quad (\text{C3})$$

Introducing the $m \times m$ matrix d Green function

$$G_{ij\sigma}^d(\epsilon + i\eta) = \int_{-\infty}^{\infty} G_{ij\sigma}^d(t, t') e^{i\epsilon(t-t')} dt, \quad (\text{C4})$$

$$G_{ij\sigma}^d(t, t') = -\theta(t-t') \langle \{ d_{i\sigma}(t), d_{j\sigma}^\dagger(t') \} \rangle, \quad (\text{C5})$$

together with the two “vector” quantities

$$v_j(\epsilon + i\eta) = t_j + t_c V_{hj} G_{\vec{R}_s, \vec{R}_j}(\epsilon + i\eta), \quad (\text{C6})$$

$$u_j(\epsilon + i\eta) = t_j + t_c V_{hj} G_{\vec{R}_j, \vec{R}_s}(\epsilon + i\eta), \quad (\text{C7})$$

the retarded f Green function is conveniently expressed as

$$G_{f\sigma}(\epsilon + i\eta) = t_c^2 G_{\vec{R}_s, \vec{R}_s}(\epsilon + i\eta) + \sum_{i,j} v_i(\epsilon + i\eta) G_{ij\sigma}^d(\epsilon + i\eta) u_j(\epsilon + i\eta), \quad (\text{C8})$$

which has the compact matrix representation:

$$G_{f\sigma}(\epsilon + i\eta) = t_c^2 G_{\vec{R}_s, \vec{R}_s}(\epsilon + i\eta) + [v^t G_{\sigma}^d u] (\epsilon + i\eta). \quad (\text{C9})$$

All information of the adatom cluster and its many-body physics is contained within the $G_{f\sigma}$ Green function of Eq. (C8), which replaces that of Eq. (8) in the final expression for the differential conductance, Eq. (10). In particular, Eq. (8) is properly recovered in the case of just a single magnetic adatom. This permits the analysis of complicated multiple-adatom configurations in terms of the matrix d Green function of Eq. (C4).

-
- ¹ J. Li, W.-D. Schneider, R. Berndt, and B. Delley, Phys. Rev. Lett. **80**, 2893 (1998).
 - ² V. Madhavan, W. Chen, T. Jamneala, M. F. Crommie, and N. S. Wingreen, Science **280**, 567 (1998).
 - ³ D. Goldhaber-Gordon, H. Shtrikman, D. Mahalu, D. Abusch-Magder, U. Meirav, and M. A. Kastner, Nature **391**, 156 (1998); D. Goldhaber-Gordon, J. Göres, M. A. Kastner, H. Shtrikman, D. Mahalu, and U. Meirav, Phys. Rev. Lett. **81**, 5225 (1998).
 - ⁴ S. M. Cronenwett, T. H. Oosterkamp, and L. P. Kouwenhoven, Science **281**, 540 (1998).
 - ⁵ D. C. Ralph and R. A. Buhrman, Phys. Rev. Lett. **72**, 3401 (1994).
 - ⁶ U. Fano, Phys. Rev. **124**, 1866 (1961).
 - ⁷ J. Appelbaum, Phys. Rev. Lett. **17**, 91 (1966); P. W. Anderson, Phys. Rev. Lett. **17**, 95 (1966).
 - ⁸ S. Hershfield, J. H. Davies, and J. W. Wilkins, Phys. Rev. Lett. **67**, 3720 (1991); Y. Meir, N. S. Wingreen, and P. A. Lee, Phys. Rev. Lett. **70**, 2601 (1993); T. K. Ng, Phys. Rev. Lett. **70**, 3635 (1993).
 - ⁹ For a comprehensive review, see N. E. Bickers, Rev. Mod. Phys. **59**, 845 (1987).
 - ¹⁰ T. Morita and T. Horiguchi, J. Math. Phys. **12**, 986 (1971).
 - ¹¹ We use the notation of *Handbook of Mathematical Functions*, edited by M. Abramowitz and A. Stegun (Dover, New York, 1972), Sec. 17.3 for $K(\zeta)$, which differs from the one used in Ref. 10.
 - ¹² For the above form of the local conduction-electron density of states and for this set of impurity model parameters, the NCA exhausts the unitary limit for $T \approx 0.85T_K$.
 - ¹³ In dilute magnetic alloys, the electrical resistivity due to the scattering of conduction electrons off the magnetic impurities is proportional to $R(T)$, hence the term “resistivity” integral [see, e.g., N. E. Bickers, D. L. Cox, and J. W. Wilkins, Phys. Rev. B **36**, 2036 (1987), Appendix D].
 - ¹⁴ C. Woll, S. Chiang, R. J. Wilson, and P. H. Lippel, Phys. Rev. B **39**, 7988 (1989).
 - ¹⁵ D. C. Langreth, Phys. Rev. **150**, 516 (1966).
 - ¹⁶ A. Chattopadhyay, private communication.
 - ¹⁷ The competition between the Kondo effect and antiferromagnetic locking for two magnetic impurities was extensively discussed in the literature. See, e.g., B. A. Jones, C. M. Varma, and J. W. Wilkins, Phys. Rev. Lett. **61**, 125 (1988); I. Affleck and A. W. W. Ludwig, Phys. Rev. Lett. **68**, 1046 (1992); I. Affleck, A. W. W. Ludwig, and B. A.

Jones, Phys. Rev. B **52**, 9528 (1995); J. B. Silva, W. L. C. Lima, W. C. Oliveira, J. L. N. Mello, L. N. Oliveira, and J. W. Wilkins, Phys. Rev. Lett. **76**, 275 (1996).
¹⁸ W. Chen, T. Jamneala, V. Madhavan, and M. F. Crommie, Phys. Rev. B **60**, 8529 (1999).